ADVANCED ENERGY MATERIALS

Supporting Information

for *Adv. Energy Mater.*, DOI 10.1002/aenm.202204370

Beyond Protocols: Understanding the Electrical Behavior of Perovskite Solar Cells by Impedance Spectroscopy

Elnaz Ghahremanirad, Osbel Almora, Sunil Suresh, Amandine A. Drew, Towhid H. Chowdhury and Alexander R. Uhl**

WILEY-VCH

Supporting Information

Beyond Protocols: Understanding the Electrical Behavior of Perovskite Solar Cells by Impedance Spectroscopy

Elnaz Ghahremanirad[1], Osbel Almora[2], Sunil Suresh[1], Amandine A. Drew[1], Towhid H. Chowdhury[1], Alexander R. Uhl[1*]*

Table S1. The most recent and relevant review articles on IS and PSCs.

Year	Protocols	Device	Model/Theory	Recommended content complementing this work	Group/Institution	Ref.
2010	ECIS	DSSCs	EC	Introduction to IS and basic ECs	INAM	[1]
2014	ECIS	DSSCs	EC	Analyzing the impedance response of ZnO-based DSSC	UKM	[2]
2017	ECIS, OCRIS	PSCs	EC	Introduction to several ECs and the impedance Bode plots in PSCs	M2N	[3]
2018	ECIS, MS, OCRIS	PSCs	EC, DD	Discussion on ionic distributions via DD simulation, studying time, frequency, and capacitive response including current-voltage hysteresis of PSCs	INAM	[4]
2018	ECIS, OCRIS	PSCs	EC	Studying the influence of ETL morphology on charge extraction in perovskites via IS	BCMaterials	[5]
2018	ECIS	PSCs	EC	Perform IS under different light intensities at a fixed voltage	GREEN	[6]
2019	ECIS	DSSCs, PSCs, polymer, QD solar	EC	IS characterization of four different photovoltaic devices: DSSCs, PSCs, polymer and QD solar cells	BIT	[7]

		cells				
2019	ECIS	DSSCs, PSCs, OSCs	EC	Methods for IS measurements and analyses, and explanation of different circuit elements	HIMS	[8]
2019	ECIS	PSCs	EC	Studying the dynamic behaviors at the interfaces of perovskite using IS	INAM	[9]
2020	ECIS	PSCs	EC	Investigating HTL-free PSCs using IS	CAM	[10]
2020	ECIS	PSCs	EC	The impact of adding a 2D perovskite layer at HTM/3D perovskite interface was studied by IS	CAM	[11]
2020	ECIS	PSCs	EC, DD	Pointing out to the importance of including ion distribution in IS modeling	GREEN	[12]
2020	ECIS	DSSCs, PSCs, QD solar cells, etc.	EC	EIS for studying metal oxide electrodes	Farnum	[13]
2021	ECIS	PSCs	EC	The characterization of metal oxide charge transport layers	HKU	[14]
2021	ECIS, CS	Single crystal PSCs	EC	Using IS for to distinguish different relaxation processes occurring in single crystal perovskites	IPV	[15]

2021	ECIS, OCRIS	Regular planar PSC	EC	The origin of low frequency resistance	IPC PAS	[16]
2021	ECIS	PSCs	EC	The significance of ECs for explaining impedance response	INAM	[17]
2022	ECIS	PSCs	EC	A general equivalent circuit comprised of low and high frequency parts	FEP	[18]
This work	ECIS, OCRIS, LIMIS	PSCs	EC, DD	Different protocols and theories for impedance spectroscopy analysis	LSEF	-

Abbreviations: **INAM**, Institute of Advanced Materials; **UKM**, Universiti Kebangsaan Malaysia; **M2N**, Molecular Materials and Nanosystems; **BCMaterials**, Basque Center for Materials, Applications and Nanostructures; **GREEN**, Center for Green Research on Energy and Environmental Materials; **BIT**, Beijing Institute of Technology; **HIMS**, Van't Hoff Institute for Molecular Sciences; **CAM**, Center for Advanced Materials; **Farnum**, Inorganic Chemistry for Renewable Energy Conversion and Storage; **HKU**, The University of Hong Kong; **IPV**, Institute for Photovoltaics; **IPC PAS**, The Institute of Physical Chemistry of the Polish Academy of Sciences; **FEP,** Electron Beam and Plasma Technology; **LSEF**, Laboratory for Solar Energy and Fuels

Table S2. The trap densities, activation energies, and PCEs for different PSCs resulted from TAS/DLTS measurements. The symbols correspond to the data points on Figure 4.

Symbol	Cell structure	Bandgap (eV)	Trap density (cm^{-3})	Activation energy (eV)	PCE (%)	Ref.
	Glass/ITO/NiO_x(PEDOT:PSS)/$(FASnI_3)_{0.6}(MAPbI_3)_{0.4}$/$PC_{61}BM$/$C_{60}$/TmPyPB/Ag	1.2	1×10^{16}	0.45	9.03	[19]
*	ITO/AZO NPs/PCBM/$MAPbI_3$/Spiro-OMeTAD/MoO_x/Al	1.5	5.9×10^{15}	0.355	13	[20]
	ITO/AZO NPs/$MAPbI_3$/Spiro-OMeTAD/MoO_x/Al	1.5	1.8×10^{16}	0.487	17	
	Glass/FTO/$MAPbI_3$ (stoichiometric)/PCBM/BCP/Ag	1.5	1.95×10^{16}	0.44	12.53	
*	Glass/FTO/$MAPbI_3$ (3% MAI)/PCBM/BCP/Ag	1.5	2.94×10^{16}	0.46	N/A	[21]
*	Glass/FTO/$MAPbI_3$ (2% MAI)/PCBM/BCP/Ag	1.5	2.42×10^{16}	0.46	N/A	
*	Glass/FTO/$(FAPbI_3)_{0.97}(MAPbBr_3)_{0.03}$/Spiro-OMeTAD/Au	N/A	1.94×10^{15}	N/A	N/A	[22]
	Glass/FTO/$(FAPbI_3)_{0.97}(MAPbBr_3)_{0.03}$ (meta-FPEAI)/Spiro-OMeTAD/Au	1.51°	1.13×10^{15}			
	$MAPbI_{3-x}Cl_x$	1.55	1×10^{17}	0.16	N/A	[23]
*	ITO/PTAA/$Cs_{0.05}(MA_{0.08}FA_{0.92})_{0.95}Pb(I_{0.92}Br_{0.08})_3$/$C_{60}$/BCP/Cu	1.56	N/A	0.32	N/A	[24]
	ITO/2PACz/$Cs_{0.18}FA_{0.82}PbI_3$/C60/BCP/Ag	1.57	3.7×10^{15}	0.696	22.7	[25]
	Glass/FTO/mp-TiO_2/$(FAPbI_3)_{0.85}(MAPbBr_3)_{0.15}$/HTM/Au	1.58	2×10^{15}	0.68	20.2	[26]
*		1.58	6×10^{15}	0.76	N/A	
*		1.58	8.2×10^{15}	0.81	N/A	
	Glass/ITO/PEDOT:PSS/$MAPbI_3$/$PC_{61}BM$/C_{60}/BCP/Ag	1.6	1×10^{16}	0.13	10.05	[19]
	ITO/TiO_2-Cl/$Cs_{0.05}MA_{0.15}FA_{0.8}Pb(I_{0.75}Br_{0.25})_3$/Spiro-OMeTAD/Au	1.65	1.1×10^{16}	0.11	20.7	[27]

■	ITO/TiO_2-Cl/$Cs_{0.2}FA_{0.8}Pb(I_{0.75}Br_{0.25})_3$/Spiro-OMeTAD/Au	1.67	6×10^{15}	0.095	17.6	[27]
*		1.67	2.1×10^{16}	0.18	N/A	
*	FTO/c-TiO_2/$CsPbI_3$/Spiro-OMeTAD/MoO_3/Au	1.7	8.63×10^{15}	N/A	15.71	[28]
+	FTO/c-TiO_2/NGBr- $CsPbI_3$ (ABA)/Spiro-OMeTAD/MoO_3/Au	1.7	3.75×10^{15}	N/A	18.27	
*	ITO/$MAPbBr_3$ (single crystalline)/MoO_3/Au/Ag	2	5.8×10^{9}	N/A	N/A	[29]

N/A: Not available

° Extracted from the external quantum efficiency (EQE) plot.

* Reported for further information, not included in Figure 4.

Abbreviation: **PEDOT: PSS**, Poly(3,4-ethylene dioxythiophene) polystyrene sulfonate; **$PC_{61}BM$**, [6,6]-Phenyl-C61-butyric acid methyl ester; **TmPyPB**, 1,3,5-Tris(3-pyridyl-3-phenyl)benzene; **AZO NPs**, aluminum doped zinc oxide nanoparticles; **PCBM**, phenyl-C60-butyric acid methyl ester; **Spiro-OMeTAD**, 2,2',7,7'-Tetrakis[N,N-di(4-methoxyphenyl)amino]-9,9'-spirobifluorene; **MoO_x**, Molybdenum oxide, **BCP**, Bathocuproine; **MAI**, Methylammonium iodide; **FPEAI**, Fluorinated phenylethylamine hydroiodide; **2PACz**, [2-(9H-carbazol-9-yl)ethyl]phosphonic acid, **PTAA**, poly(triaryl amine); **mp-TiO_2**, Mesoporous TiO_2; **c-TiO_2**, compact TiO_2; **NGBr**, Neostigmine bromide; **ABA**, 4–aminobenzoic acid.

Table S3. The perovskite solar cell configuration of the samples presented in Figure 6 of the manuscript.

Sample No.	Cell structure	Ref.
1	FTO/TiO_2/$MAPbI_3$/Spiro–OMeTAD/Au	[30]
2	FTO/TiO_2/$MAPbI_3$/Spiro–OMeTAD/Au	[31]
3	FTO/TiO_2/$CS_{0.1}FA_{0.74}MA_{0.13}PbI_{2.48}Br_{0.39}$/Spiro–OMeTAD/Au	[30]
4	ITO/SnO_2/PMMA(PCBM)/$Cs_{0.05}MA_{0.1}FA_{0.85}PbI_{2.55}Br_{0.45}$/PDCBT/Ta–$WO_x$/Au	[32]
5	ITO/SnO_2/ $Cs_{0.05}MA_{0.1}FA_{0.85}PbI_{2.55}Br_{0.45}$/PDCBT/Ta–$WO_x$/Au	
6	ITO/SnO_2/$Cs_{0.15}FA_{0.85}PbI_3$/PDCBT/Ta–WO_x/Au	

Abbreviation: **FTO**, Fluorine-doped Tin Oxide; **ITO**, Indium tin oxide; **SnO_2**, Tin oxide; **PMMA**, Polymethylmethacrylate; **PDCBT**, Poly[5,5′-bis(2-butyloctyl)-(2,2′-bithiophene)-4,4′-dicarboxylate-alt-5,5′-2,2′-bithiophene; **Ta–WO_x**, Tantalum–doped tungsten oxide;

Table S4. Selected examples of electrical equivalent circuits for perovskite solar cells with their respective cell structure and impedance response.

Year	Cell Structure	Measurement condition	Impedance plot	Group	Ref.
2015	Glass/FTO/TiO_2/$MAPbI_3$/Spiro-OMeTAD/Au	Under illumination intensity of 273 W m^{-2} at V_{oc}	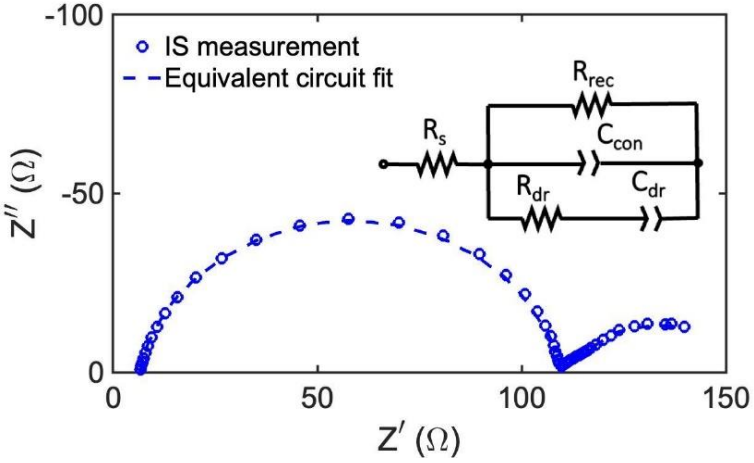	Monash University	[31]

2018	Glass/ITO/ETL/$FA_{0.95}Cs_{0.05}PbI_3$/Spiro-OMeTAD/Au	In the dark at V_{oc}	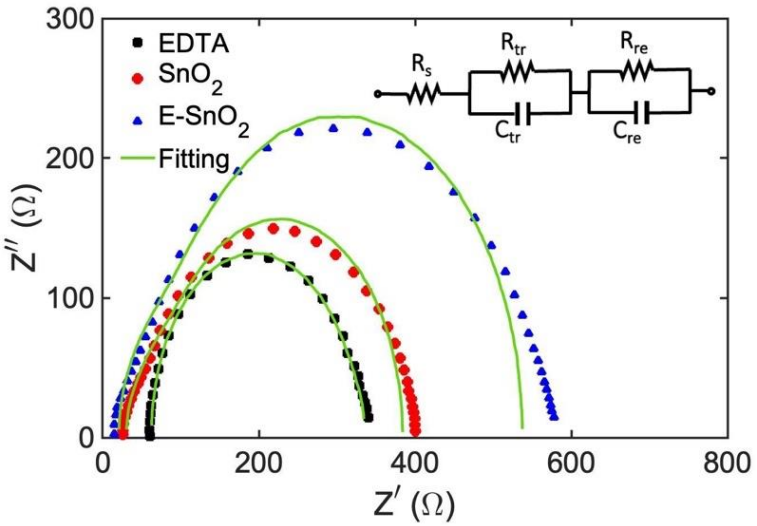	CEHMS	[33]
2019	Glass/FTO/c-TiO_2/m-TiO_2/$MAPbBr_3$/Au	In the dark at the DC bias of 0 - 0.2 V (simulation)	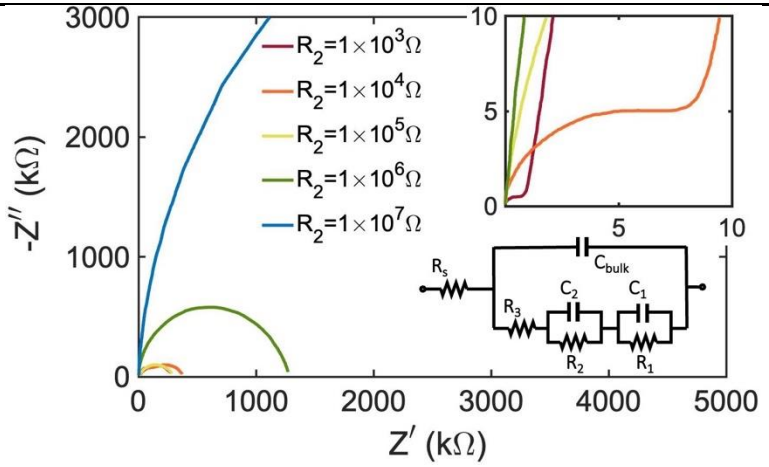	INAM	[34]

2019	FTO/SnO_2/$MAPbI_3$/Spiro-OMeTAD/Au	In the dark at different forward biases	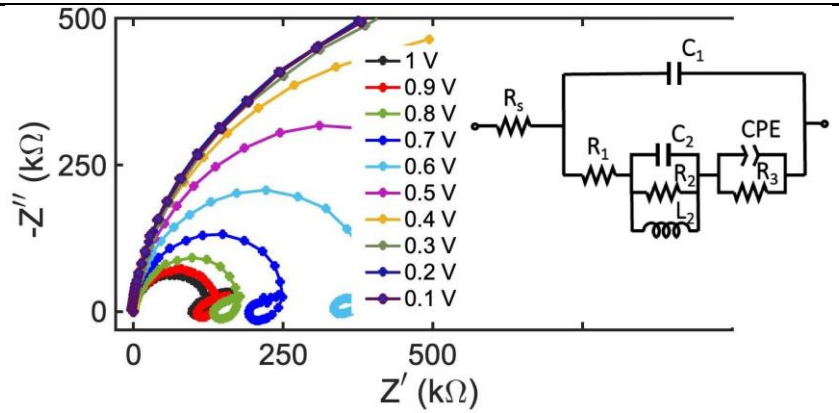	Hersam	[35]
2019	Glass/FTO/TiO_2/$FA_{0.85}MA_{0.15}PbI_3$ (CsAc)/Spiro-OMeTAD/Au	In the dark at V_{oc}	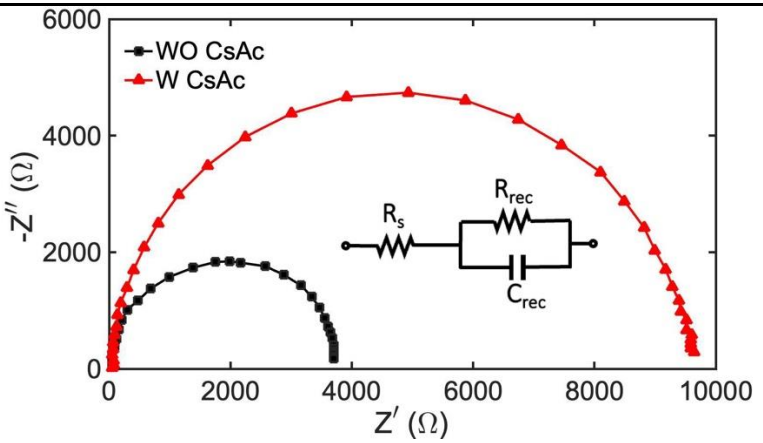	Dalian Institute of Chemical Physics	[36]

2020	FTO/c-TiO_2/m-TiO_2/([$(FA_{0.83}MA_{0.17})Cs_{0.05}$]Pb($I_{0.83}Br_{0.17}$)$_3$)/PEAI-based 2D layer/Spiro-OMeTAD/Au	In the dark under short-circuit condition	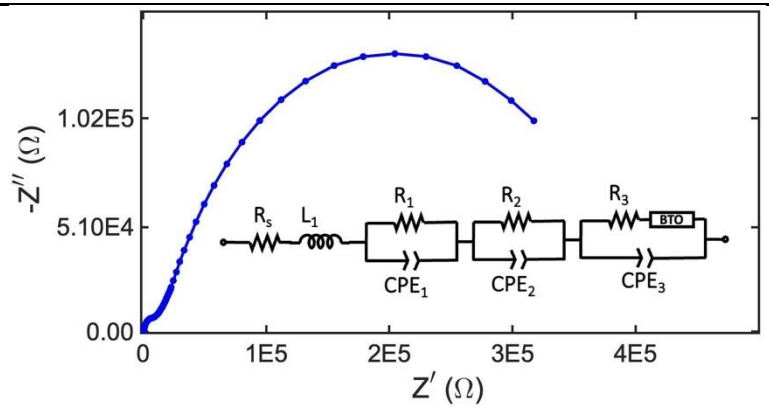	CAM	[11]
2020	Glass/ ITO/SnO_2/ $Cs_{0.05}(FAPbI_3)_{0.85}(MAPbBr_3)_{0.15}$/Spiro-OMeTAD/Ag	In the dark at a DC bias of 0.9 V	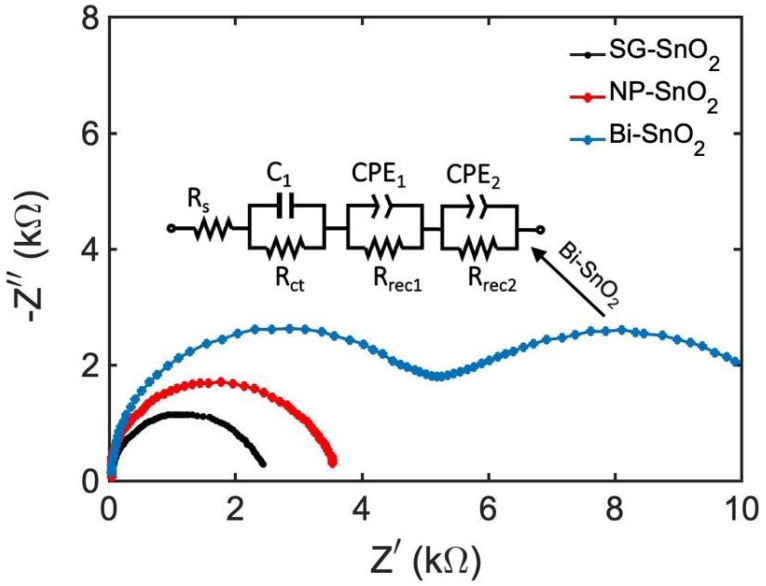	*LANL-CBNU*	[37]

Abbreviations: **CEHMS**, Center for Energy Harvesting Materials and Systems; **INAM**, Institute of Advanced Materials; **CAM**, Center for Advanced Materials; **LANL-CBNU**, LANL-CBNU Engineering Institute Korea.

Table S5. Selected DD-based simulators including Driftfusion, IonMonger, SCAPS, and SETFOS. FEM: Finite Element method; FDM: Finite Difference Method; MC: Monte-Carlo; BC: Boundary conditions; F–D: Fermi Dirac; WKB: Wentzel Kramers Brillouin; OLED: Organic Light Emitting Diode.

Parameters	Driftfusion [38-39]	IonMonger [40]	SCAPS [41]	SETFOS [42-45]
Numerical method	FEM	FEM and adaptive time-stepping	FDM	MC-based
The number of layers	Multiple	Three	Multiple	Three
Charge carrier species	Electrons, holes, anions, and cations	Electrons, holes, single ionic species	Electrons, holes	Electrons, holes, anions
Boundary conditions	Dirichlet conditions for electrostatic potential, Neumann conditions for charge carriers, zero flux density BCs for mobile ions at the electrode boundaries	Ohmic BCs on the external boundaries with metal contacts, Dirichlet BCs for electric potential and electron (hole) density in ETL(HTL)	BCs at interfaces and contacts	Neumann BC of zero flux (no ions can enter or leave the perovskite layer), Fixed electronic charge carrier densities in the bulk.
Initial assumptions	Homogeneous; isotropic;	Homogeneous and isotropic, quasi–equilibrium. Assumes	Homogeneous, isotropic, and in thermodynamic	Isotropic but may not be homogeneous due to the

	quasi–thermal equilibrium Charge carriers are governed by the F–D distribution function; Energy bands are described by the effective mass approximation. Considers a discrete interlayer interface approach for heterojunctions.	that the charge carriers are governed by either F–D or Boltzmann distribution.	equilibrium. WKB approximation to calculate tunnel probabilities. Includes models for defects and interfaces.	presence of traps and impurities; In thermal equilibrium. Assumes that charge carriers are governed by Maxwell-Boltzmann statistics.
Derived parameters	Doping density, carrier concentration, and current density, quasi–Fermi levels, impedance response, etc. Can simulate transient and steady-state behavior as well as optical properties such as absorption.	Open-circuit voltage, short-circuit current, and fill factor, ideality factor, doping density impedance response, etc. Can simulate transient and steady-state behavior.	Current-voltage curve, spectral response, capacitance measurements *C–V* and *C–f*, optical properties such as absorption and reflectance.	Carrier concentration, electric field, and current density. Can simulate transient and steady-state behavior, as well as the density of states and the mobility of charge carriers.

Parameters for impedance simulation	AC voltage amplitude, DC voltage amplitude, voltage period, frequency, frequency points, time-dependent illumination intensity	Minimum and maximum frequency, DC applied voltage, AC voltage amplitude, the number of frequency points, time-dependent illumination intensity, the number of complete periods to simulate the impedance response, numerical simulation of IS over the timescales of seconds to minutes	DC voltage amplitude, voltage period, frequency, frequency points	
Device	Semiconductor devices with mixed ionic-electronic conducting layers	PSCs	Solar cells, Organic electronic devices	Solar cells, OLEDs

Table S6. Device parameters used in DD modelling.

Parameter	Value			Description
Perovskite layer				
t (nm)	300	500	500	Layer thickness
ε_r	20	20	62	Permittivity
E_g(eV)	1.6	1.6	1.6	Bandgap
χ (eV)	–	–	3.9	Electron affinity
μ_n ($cm^2V^{-1}s^{-1}$)	~19	20	1	Electron mobility
μ_p ($cm^2V^{-1}s^{-1}$)	~19	20	1	Hole mobility
D_n ($cm^2\ s^{-1}$)	5×10^{-1}	5.2×10^{-1}	2.6×10^{-2}	Electron diffusion coefficient
D_p ($cm^2\ s^{-1}$)	5×10^{-1}	5.2×10^{-1}	2.6×10^{-2}	Hole diffusion coefficient
N_A (cm^{-3})	–	–	4×10^{17}	Acceptor doping density
N_D (cm^{-3})	–	–	4×10^{17}	Donor doping density
N_c (cm^{-3})	8.1×10^{18}	1×10^{20}	8×10^{18}	Conduction band density of states
N_v (cm^{-3})	5.8×10^{18}	1×10^{20}	6×10^{18}	Valence band density of states
N_{ion}	1.6×10^{19}	1×10^{19}	$1(2)\times10^{18}$	Mobile ionic density
D_{ion}	1×10^{-12}	–	$1\times10^{-9(-11)}$	Ionic diffusion coefficient
σ_n (cm^{-2})	–	–	1×10^{-15}	SRH electron cross section
σ_p (cm^{-2})	–	–	1×10^{-17}	SRH hole cross section
N_t (cm^{-3})	–	–	1×10^{14}	Trap density
E_t (eV)	–	–	Mid-gap	Trap energy
Electron transport layer				
t	100	200	120	Layer thickness
ε_r	20	20	55	Permittivity
E_g(eV)	–	1.6	3.39	Bandgap
χ (eV)	–	–	4.1	Electron affinity
μ_n ($cm^2V^{-1}s^{-1}$)	–	20	0.1	Electron mobility
μ_p ($cm^2V^{-1}s^{-1}$)	–	0.02	0.1	Hole mobility
D_n ($cm^2\ s^{-1}$)	5.14×10^{-3}	5.2×10^{-1}	2.6×10^{-3}	Electron diffusion coefficient
D_p ($cm^2\ s^{-1}$)	–	5.2×10^{-4}	2.6×10^{-3}	Hole diffusion coefficient
N_A (cm^{-3})	–	–	–	Acceptor doping density
N_D (cm^{-3})	–	3×10^{17}	1×10^{17}	Donor doping density

N_c (cm^{-3})	–	1×10^{20}	8×10^{18}	Conduction band density of states
N_v (cm^{-3})	–	1×10^{20}	6×10^{18}	Valence band density of states
Hole transport layer				
t	300	200	200	Layer thickness
ε_r	3	20	3	Permittivity
E_g(eV)	–	1.6	3	Bandgap
χ (eV)	–	–	2.1	Electron affinity
μ_n ($cm^2V^{-1}s^{-1}$)	–	0.02	0.1	Electron mobility
μ_p ($cm^2V^{-1}s^{-1}$)	0.001	20	0.1	Hole mobility
D_n ($cm^2\ s^{-1}$)	–	5.2×10^{-4}	2.6×10^{-3}	Electron diffusion coefficient
D_p ($cm^2\ s^{-1}$)	2.57×10^{-5}	5.2×10^{-1}	2.6×10^{-3}	Hole diffusion coefficient
N_A (cm^{-3})	–	3×10^{17}	1×10^{19}	Acceptor doping density
N_D (cm^{-3})	–	–	–	Donor doping density
N_c (cm^{-3})	–	1×10^{20}	8×10^{18}	Conduction band density of states
N_v (cm^{-3})	–	1×10^{20}	6×10^{18}	Valence band density of states
Ref.	[46]	[39]	[47]	

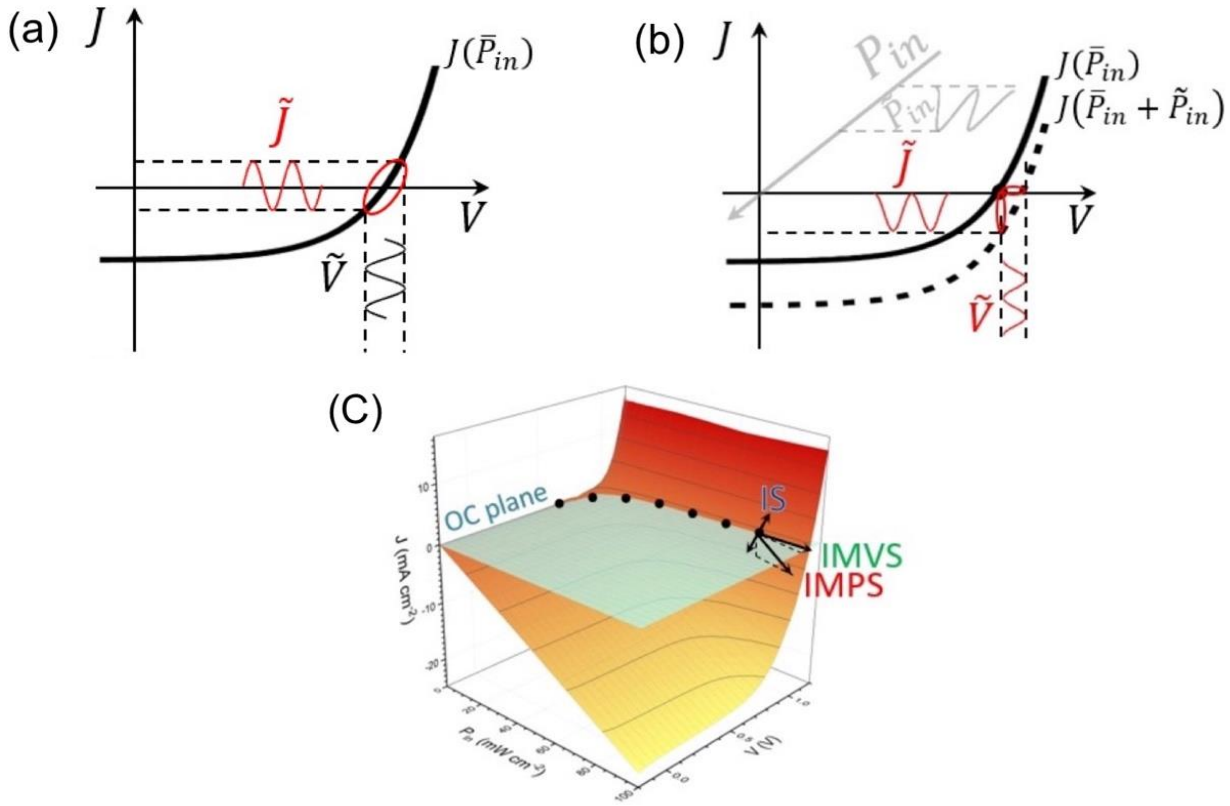

Figure S1. Schematized impedance characterization of a photovoltaic solar cell in two–dimensional $J-V$ representations for (a) IS and (b) IMPS and IMVS that lead to LIMIS. The thick dashed line in (b) is the projection of the perturbed $J(V,P_{in})$ curve in three–dimensional representation, as in (c). In (c) the three experimental measurements are illustrated at an OC point in the interception between the OC plane and the experimental $\bar{J}(\bar{V},\bar{P}_{in})$ surface of a PSC. Reproduced with permission from, [32] Copyright 2020, Elsevier.

References

[1] F. Fabregat-Santiago in *Impedance spectroscopy: a general introduction and application to dye-sensitized solar cells*, EPFL Press, **2010**, pp. 477-574. https://www.researchgate.net/publication/282677277_Impedance_Spectroscopy_A_General_Introduction_and_Application_to_Dye-Sensitized_Solar_Cells.

[2] A. Omar and H. Abdullah, Electron transport analysis in zinc oxide-based dye-sensitized solar cells: a review, *Renew. Sust. Energ. Rev.* **2014**, *31*, 149-157.

[3] A. Todinova, L. Contreras-Bernal, M. Salado, S. Ahmad, N. Morillo, J. Idígoras and J.A. Anta, Towards a universal approach for the analysis of impedance spectra of perovskite solar cells: equivalent circuits and empirical analysis, *ChemElectroChem* **2017**, *4*, 2891-2901.

[4] P. Lopez-Varo, J.A. Jiménez-Tejada, M. García-Rosell, S. Ravishankar, G. Garcia-Belmonte, J. Bisquert and O. Almora, Device physics of hybrid perovskite solar cells: theory and experiment, *Adv. Energy Mater.* **2018**, *8*, 1702772.

[5] M. Salado, L. Calió, L. Contreras-Bernal, J. Idígoras, J.A. Anta, S. Ahmad and S. Kazim, Understanding the influence of interface morphology on the performance of perovskite solar cells, *Materials* **2018**, *11*, 1073.

[6] X. Chen, Y. Shirai, M. Yanagida and K. Miyano, Effect of light and voltage on electrochemical impedance spectroscopy of perovskite solar cells: an empirical approach based on modified randles Circuit, *J. Phys. Chem. C* **2019**, *123*, 3968-3978.

[7] S. Ali, S. Chang, M. Imran, Q. Shi, Y. Chen and H. Zhong, Impedance Spectroscopy: A Versatile Technique to Understand Solution-Processed Optoelectronic Devices, *Phys. Status Solidi RRL* **2019**, *13*, 1800580.

[8] E. Von Hauff, Impedance spectroscopy for emerging photovoltaics, *J. Phys. Chem. C* **2019**, *123*, 11329-11346.

[9] H. Wang, A. Guerrero, A. Bou, A.M. Al-Mayouf and J. Bisquert, Kinetic and material properties of interfaces governing slow response and long timescale phenomena in perovskite solar cells, *Energy Environ. Sci.* **2019**, *12*, 2054-2079.

[10] S.M. Abdulrahim, Z. Ahmad, J. Bahadra and N.J. Al-Thani, Electrochemical Impedance Spectroscopy Analysis of Hole Transporting Material Free Mesoporous and Planar Perovskite Solar Cells, *Nanomaterials* **2020**, *10*, 1635.

[11] S.M. Abdulrahim, Z. Ahmad, J. Bhadra and N.J. Al-Thani, Long-term stability analysis of 3D and 2D/3D hybrid perovskite solar cells using electrochemical impedance spectroscopy, *Molecules* **2020**, *25*, 5794.

[12] K. Miyano, M. Yanagida and Y. Shirai, Impedance Spectroscopy Revisited, *Adv. Energy Mater.* **2020**, *10*, 1903097.

[13] A.R. Bredar, A.L. Chown, A.R. Burton and B.H. Farnum, Electrochemical impedance spectroscopy of metal oxide electrodes for energy applications, *ACS Appl. Energy Mater.* **2020**, *3*, 66-98.

[14] Y. Wang, A.B. Djurisic, W. Chen, F. Liu, R. Cheng, S.-P. Feng, A.M.C. Ng and Z. He, Metal oxide charge transport layers in perovskite solar cells-optimising low temperature processing and improving the interfaces towards low temperature processed, efficient and stable devices, *Journal of Physics: Energy* **2020**.

[15] M.A. Afroz, C.A. Aranda, N.K. Tailor, Yukta, P. Yadav, M.M. Tavakoli, M. Saliba and S. Satapathi, Impedance Spectroscopy for Metal Halide Perovskite Single Crystals: Recent Advances, Challenges, and Solutions, *ACS Energy Lett.* **2021**, *6*, 3275-3286.

[16] D. Prochowicz, S. Trivedi, N. Parikh, M. Saliba, A. Kalam, M.M. Tavakoli and P. Yadav, In the Quest of Low Frequency Impedance Spectra of Efficient Perovskite Solar Cells, *Energy Technol.* **2021**.

[17] A. Guerrero, J. Bisquert and G. Garcia-Belmonte, Impedance Spectroscopy of Metal Halide Perovskite Solar Cells from the Perspective of Equivalent Circuits, *Chem. Rev.* **2021**.

[18] E. von Hauff and D. Klotz, Impedance spectroscopy for perovskite solar cells: characterisation, analysis, and diagnosis, *J. Mater. Chem. C* **2022**, *10*, 742-761.

[19] G.R. Neupane, M. Bamidele, V. Yeddu, D.Y. Kim and P. Hari, Negative capacitance and hysteresis in encapsulated $MAPbI_3$ and lead–tin (Pb–Sn) perovskite solar cells, *J. Mater. Res.* **2022**, *37*, 1357-1372.

[20] Q. Dong, C.H.Y. Ho, H. Yu, A. Salehi and F. So, Defect passivation by fullerene derivative in perovskite solar cells with aluminum-doped zinc oxide as electron transporting layer, *Chem. Mater.* **2019**, *31*, 6833-6840.

[21] B. Chen, H. Hu, T. Salim and Y.M. Lam, A facile method to evaluate the influence of trap densities on perovskite solar cell performance, *J. Mater. Chem. C* **2019**, *7*, 5646-5651.

[22] X. Ren, B. Zhang, L. Zhang, J. Wen, B. Che, D. Bai, J. You, T. Chen and S. Liu, Deep-Level Transient Spectroscopy for Effective Passivator Selection in Perovskite Solar Cells to Attain High Efficiency over 23%, *ChemSusChem* **2021**, *14*, 3182-3189.

[23] O. Almora, M. García-Batlle and G. Garcia-Belmonte, Utilization of temperature-sweeping capacitive techniques to evaluate band gap defect densities in photovoltaic perovskites, *J. Phys. Chem. Lett.* **2019**, *10*, 3661-3669.

[24] X. Zheng, Y. Hou, C. Bao, J. Yin, F. Yuan, Z. Huang, K. Song, J. Liu, J. Troughton and N. Gasparini, Managing grains and interfaces via ligand anchoring enables 22.3%-efficiency inverted perovskite solar cells, *Nat. Energy* **2020**, *5*, 131-140.

[25] S. Gharibzadeh, P. Fassl, I.M. Hossain, P. Rohrbeck, M. Frericks, M. Schmidt, M.R. Khan, T. Abzieher, B.A. Nejand and F. Schackmar, Two birds with one stone: dual grain-boundary and interface passivation enables> 22% efficient inverted methylammonium-free perovskite solar cells, *Energy Environ. Sci.* **2021**, *14*, 5875-5893.

[26] S. Heo, G. Seo, Y. Lee, M. Seol, S.H. Kim, D.J. Yun, Y. Kim, K. Kim, J. Lee and J. Lee, Origins of high performance and degradation in the mixed perovskite solar cells, *Adv. Mater.* **2019**, *31*, 1805438.

[27] H. Tan, F. Che, M. Wei, Y. Zhao, M.I. Saidaminov, P. Todorović, D. Broberg, G. Walters, F. Tan and T. Zhuang, Dipolar cations confer defect tolerance in wide-bandgap metal halide perovskites, *Nat. Commun.* **2018**, *9*, 1-10.

[28] Y. Wang, G. Chen, D. Ouyang, X. He, C. Li, R. Ma, W.J. Yin and W.C. Choy, High phase stability in $CsPbI_3$ enabled by Pb–I octahedra anchors for efficient inorganic perovskite photovoltaics, *Adv. Mater.* **2020**, *32*, 2000186.

[29] D. Shi, V. Adinolfi, R. Comin, M. Yuan, E. Alarousu, A. Buin, Y. Chen, S. Hoogland, A. Rothenberger and K. Katsiev, Low trap-state density and long carrier diffusion in organolead trihalide perovskite single crystals, *Science* **2015**, *347*, 519-522.

[30] O. Almora, K.T. Cho, S. Aghazada, I. Zimmermann, G.J. Matt, C.J. Brabec, M.K. Nazeeruddin and G. Garcia-Belmonte, Discerning recombination mechanisms and ideality factors through impedance analysis of high-efficiency perovskite solar cells, *Nano Energy* **2018**, *48*, 63-72.

[31] A.R. Pascoe, N.W. Duffy, A.D. Scully, F. Huang and Y.-B. Cheng, Insights into planar CH3NH3PbI3 perovskite solar cells using impedance spectroscopy, *J. Phys. Chem. C* **2015**, *119*, 4444-4453.

[32] O. Almora, Y. Zhao, X. Du, T. Heumueller, G.J. Matt, G. Garcia-Belmonte and C.J. Brabec, Light intensity modulated impedance spectroscopy (LIMIS) in all-solid-state solar cells at open-circuit, *Nano Energy* **2020**, *75*, 104982.

[33] D. Yang, R. Yang, K. Wang, C. Wu, X. Zhu, J. Feng, X. Ren, G. Fang, S. Priya and S.F. Liu, High efficiency planar-type perovskite solar cells with negligible hysteresis using EDTA-complexed SnO_2, *Nat. Commun.* **2018**, *9*, 1-11.

[34] C. Aranda, J. Bisquert and A. Guerrero, Impedance spectroscopy of perovskite/contact interface: Beneficial chemical reactivity effect, *J. Chem. Phys.* **2019**, *151*, 124201.

[35] V.K. Sangwan, M. Zhu, S. Clark, K.A. Luck, T.J. Marks, M.G. Kanatzidis and M.C. Hersam, Low-frequency carrier kinetics in perovskite solar cells, *ACS Appl. Mater. Interfaces.* **2019**, *11*, 14166-14174.

[36] S. Yuan, Y. Cai, S. Yang, H. Zhao, F. Qian, Y. Han, J. Sun, Z. Liu and S. Liu, Simultaneous cesium and acetate coalloying improves efficiency and stability of $FA_{0.85}MA_{0.15}PbI_3$ perovskite solar cell with an efficiency of 21.95%, *Sol. RRL* **2019**, *3*, 1900220.

[37] H.B. Lee, N. Kumar, M.M. Ovhal, Y.J. Kim, Y.M. Song and J.W. Kang, Dopant-Free, Amorphous–Crystalline Heterophase SnO_2 Electron Transport Bilayer Enables> 20% Efficiency in Triple-Cation Perovskite Solar Cells, *Adv. Funct. Mater.* **2020**, *30*, 2001559.

[38] P. Calado, I. Gelmetti, B. Hilton, M. Azzouzi, J. Nelson and P.R.F. Barnes, Driftfusion: an open source code for simulating ordered semiconductor devices with mixed ionic-electronic conducting materials in one dimension, *Journal of Computational Electronics* **2022**, *21*, 960-991.

[39] D. Moia, I. Gelmetti, P. Calado, W. Fisher, M. Stringer, O. Game, Y. Hu, P. Docampo, D. Lidzey and E. Palomares, Ionic-to-electronic current amplification in hybrid perovskite solar cells: ionically gated transistor-interface circuit model explains hysteresis and impedance of mixed conducting devices, *Energy Environ. Sci.* **2019**, *12*, 1296-1308.

[40] W. Clarke, L.J. Bennett, Y. Grudeva, J.M. Foster, G. Richardson and N.E. Courtier, IonMonger 2.0: software for free, fast and versatile simulation of current, voltage and impedance response of planar perovskite solar cells, *Journal of Computational Electronics* **2023**, *22*, 364-382.

[41] M. Burgelman, P. Nollet and S. Degrave, Modelling polycrystalline semiconductor solar cells, *Thin Solid Films* **2000**, *361-362*, 527-532.

[42] S. Altazin, C. Kirsch, E. Knapp, A. Stous and B. Ruhstaller, Refined drift-diffusion model for the simulation of charge transport across layer interfaces in organic semiconductor devices, *J. Appl. Phys.* **2018**, *124*, 135501.

[43] C. Vael, S. Jenatsch, S. Züfle, F. Nüesch and B. Ruhstaller, Scrutinizing thermally stimulated current transients originating from trapped charges in organic semiconductors: A drift-diffusion study, *J. Appl. Phys.* **2022**, *131*, 205702.

[44] M.S. Salem, A. Shaker, M. Abouelatta and A. Saeed in *Full Optoelectronic Simulation of Lead-Free Perovskite/Organic Tandem Solar Cells, Vol. 15* **2023**.

[45] M.T. Neukom, A. Schiller, S. Züfle, E. Knapp, J. Ávila, D. Pérez-del-Rey, C. Dreessen, K.P. Zanoni, M. Sessolo and H.J. Bolink, Consistent device simulation model describing perovskite solar cells in steady-state, transient, and frequency domain, *ACS Appl. Mater. Interfaces.* **2019**, *11*, 23320-23328.

[46] A.J. Riquelme, K. Valadez-Villalobos, P.P. Boix, G. Oskam, I. Mora-Seró and J.A. Anta, Understanding equivalent circuits in perovskite solar cells. Insights from drift-diffusion simulation, *Phys. Chem. Chem. Phys.* **2022**, *24*, 15657-15671.

[47] D.A. Jacobs, H. Shen, F. Pfeffer, J. Peng, T.P. White, F.J. Beck and K.R. Catchpole, The two faces of capacitance: new interpretations for electrical impedance measurements of perovskite solar cells and their relation to hysteresis, *J. Appl. Phys.* **2018**, *124*, 225702.